

Estimating Directional Wave Spectra Properties in Nonbreaking Waves from a UAS-Mounted Multibeam Lidar

FALK FEDDERSEN,^a OLAVO B. MARQUES,^{a,b} JAMES H. MACMAHAN,^b AND ROBERT L. GRENZEBACK^a

^a *Scripps Institution of Oceanography, University of California, San Diego, La Jolla, California*

^b *Oceanography Department, Naval Postgraduate School, Monterey, California*

(Manuscript received 26 September 2023, in final form 12 January 2024, accepted 18 March 2024)

ABSTRACT: Wave spectra and directional moment measurements are of scientific and engineering interest and are routinely estimated with wave buoys. Recently, both fixed-location and uncrewed aircraft system (UAS)-mounted lidar have estimated surfzone wave spectra. However, nearshore wave statistics seaward of the surfzone have not been measured with lidar due to low return number, and nearshore directional moments have not been measured at all. We use a multibeam scanning lidar mounted on a gasoline-powered UAS to estimate wave spectra, wave slope spectra, and directional moments on the inner shelf in ≈ 10 -m water depth from an 11-min hover and compare to a collocated wave buoy. Lidar returns within circular sampling regions with varying radius R are fit to a plane and a 2D parabola, providing sea surface and slope time series. Wave spectra across the sea-swell (0.04–0.4 Hz) band are robustly estimated for $R \geq 0.8$ m. Estimating slope spectra is more challenging. Large R works well in the swell band, and smaller R works well at higher frequencies, in good agreement with a wave buoy inferred slope spectrum. Directional Fourier coefficients, estimated from wave and slope spectra and cross-spectra, are compared to a wave buoy in the sea-swell band. Larger R and the 2D parabola-fit yield better comparison to the wave buoy. Mean wave angles and directional spreads, functions of the directional Fourier coefficients, are well reproduced at $R = 2.4$ m and the 2D parabola-fit, within the uncertainties of the wave buoy. The internal consistency of the UAS-lidar-derived results and their good comparison to the Spotter wave buoy demonstrate the effectiveness of this tool for estimating wave statistics.

SIGNIFICANCE STATEMENT: Previously fixed-location or hovering lidar has been used to estimate wave spectra in the surf and swash zone where lidar returns are high due to the reflectance of foam. We present a methodology to accurately estimate wave spectra and directional properties on the inner shelf where waves are not breaking using a hovering uncrewed aircraft system with a mounted lidar. The estimated wave spectra and directional statistics are compared well with a Spotter wave buoy, demonstrating the method's robustness.

KEYWORDS: Buoy observations; Lidars/Lidar observations; Remote sensing; Unpiloted aerial systems

1. Introduction

Measurements of surface gravity wave statistics are required for both scientific research and engineering applications. Wave statistics of interest are the frequency-dependent sea surface η elevation spectra $S_\eta(f)$, on which significant wave height H_s , peak period, and mean period are based, as well as directional moments such as mean wave angle $\theta_1(f)$ and directional spread $\sigma_\theta(f)$ (Kuik et al. 1988). These directional moments are derived from the first four Fourier coefficients of the directional spectra and are denoted as $a_1(f)$, $b_1(f)$, $a_2(f)$, and $b_2(f)$ (Longuet-Higgins et al. 1963). Wave spectra and directional moments are typically derived from pitch-and-roll wave buoys (e.g., Kuik et al. 1988), collocated pressure sensor and current meter (e.g., Herbers et al. 1999), or acoustic Doppler current profiler (ADCP, e.g., Herbers and Lentz 2010), using spectra and cross-spectra of measured variables. More recently, attention has been focused on the development of inexpensive wave buoys that are either GPS-based (e.g., Herbers et al. 2012; Raghukumar et al. 2019) or inertial measurement unit (IMU)-based (e.g., Rabault et al. 2022; Feddersen et al. 2024).

Light detection and ranging (lidar) is a remote sensing tool with significant potential for studying surface gravity waves as a lidar return is a direct measure of the distance to the water surface. An aircraft-mounted single-beam scanning (rotating 360°) lidar measured the sea surface near a wave buoy, and the resulting nondirectional wave spectra were similar to buoy-estimated spectra (Hwang et al. 2000). Since then, aircraft-based lidar wave measurements have advanced significantly (e.g., Melville et al. 2016). Assuming a statistically spatially homogeneous wave field, airborne lidar observations over 10-km swaths resolved the deep-water directional spectrum at frequencies from 0.07 to 0.6 Hz or wavelengths from 314 to 4 m (Lenain and Melville 2017). An airborne single-scanning lidar estimated spatial variations of significant wave height at 1-km resolution at the mouth of the Columbia River, allowing the study of wave amplification effects (Branch et al. 2018). Airborne lidar with a single scanning beam resolves to the high wavenumber (short wavelength) portion of the wave spectrum (Lenain and Melville 2017) allowing wave slope estimation (Lenain et al. 2019) as wave slope is dominated by short waves. Wave slope variability induced by internal waves in roughly 80-m water depth was estimated at scales of 50 m (Lenain and Pizzo 2021). However, this only included slope contributions at >0.18 Hz. In the nearshore, wave spectra at lower sea-swell frequencies (longer wavelengths) are of interest. Additionally, the nearshore region has significant depth variations and

Corresponding author: Falk Feddersen, ffeddersen@ucsd.edu

DOI: 10.1175/JTECH-D-23-0129.1

© 2024 American Meteorological Society. This published article is licensed under the terms of the default AMS reuse license. For information regarding reuse of this content and general copyright information, consult the AMS Copyright Policy (www.ametsoc.org/PUBSReuseLicenses).

rapid wave transformation making the requirement of spatial homogeneity challenging.

Fixed-location lidar-based temporal sea surface elevation measurements were first performed by Irish et al. (2006). They mounted four nonscanning point-beam lidars in a rectangular grid with a horizontal spacing of 0.6–2.0 m on the Field Research Facility (FRF, North Carolina) pier 6–16 m above the water surface. Wave spectra $S_{\eta}(f)$ and significant wave heights were well reproduced, but the array spacing and instrument number were not ideal for estimating directional moments. Single-beam scanning lidars mounted on a fixed location have been used to measure the temporal t and cross-shore x varying sea surface $\eta(x, t)$ in the swash zone on sandy (Blenkinsopp et al. 2010) and gravel (Almeida et al. 2013) beaches. Blenkinsopp et al. (2010) showed that swash zone η estimated from a 905-nm wavelength lidar matched well with ultrasonic altimeters deployed in the swash zone. Using a fixed-location scanning lidar at a 1550-nm wavelength, Brodie et al. (2015) showed that lidar-derived wave setup and wave spectra matched those of pressure sensors in the inner surfzone at low grazing angles and distances 25–65 m from the lidar. A fixed-location 1550-nm lidar scanning a highly energetic, low-sloped beach compared well to a swash zone pressure sensor at ranges of 250–350 m also at low grazing angles (Fiedler et al. 2015). Three fixed-location lidars mounted on a pier were used to generate a cross-shore continuous time series of sea surface elevation across the surfzone (Martins et al. 2017). As these studies used a single-beam scanning lidar, only a single spatial direction was resolved, and directional wave information could not be estimated.

The aerated nature of water in the swash zone and surfzone is ideal for lidar reflections at all wavelengths. For nonbreaking waves, lidar returns depend on the lidar wavelength. Lidars with a wavelength near 900 nm perform far better on water surfaces than lidars at 1550 nm due to the order of magnitude smaller absorption coefficient at 905 nm (Wojtanowski et al. 2014). Thus, lidar at a 1550-nm wavelength is more limited in measuring waves seaward of the surfzone where the water surface is not aerated. A lidar with a 905-nm wavelength was able to well reproduce wavestaff-based wave observations in a laboratory (Blenkinsopp et al. 2012). Detailed observations of wave overturning have been made using a multibeam 905-nm scanning lidar in both field settings (O’Dea et al. 2021) and field-scale laboratory settings (Feddersen et al. 2023; Baker et al. 2023).

An uncrewed aircraft system (UAS) with real-time kinematic global navigation satellite systems (RTK-GNSS) positioning and video were used to study beach profile evolution with the structure from motion (Turner et al. 2016) and observe the wave speed to estimate bathymetry (Brodie et al. 2019; Lange et al. 2023). As a more direct measurement, lidar has advantages and liabilities over video. UAS with a mounted lidar is used in various mapping and surveying applications that were enabled by advances in UAS positioning (GPS and IMU) and lidar technology. One advantage of a UAS with mounted lidar is the high grazing angles, which are more conducive to returns than the low grazing angles of shore-mounted systems. Surface gravity waves and tides were estimated at a single location by an 870-nm scanning lidar at a height 6–10 m above the surface and were

validated against an in situ pressure gauge (Huang et al. 2018). Fiedler et al. (2021) extended this work with a 905-nm scanning lidar mounted on a UAS. Wave spectra within the surfzone and swash zone were estimated and validated against in situ pressure sensor data. However, observations were limited seaward of the surfzone where wave breaking did not occur, and no directional information was estimated.

In contrast to single-beam scanning lidars, multibeam scanning lidars enable two-dimensional (2D) sea surface elevation measurements, allowing for directional wave analysis with a single instrument. Here, we use a gasoline-powered UAS with a multibeam 903-nm wavelength scanning lidar payload to estimate directional wave statistics at a point location seaward of the surfzone in 10-m water depth and compare to a Spotter wave buoy. Essentially, the point-location directional wave spectral statistics estimated by the UAS-lidar are those that a wave buoy estimates. Estimating similar statistics with a phased array at multiple lags requires a statistically homogeneous wave field, which is not the case here. The UAS together with the lidar package, as well as the data collection by the collocated Spotter buoy, is described in section 2. Binning regions of different radii are defined, and the statistics of lidar returns, as well as the method for fitting the sea surface and its slope, are described in section 3. In section 4, UAS-lidar estimated time series of η and $\partial\eta/\partial x$ and bulk statistics, as well as S_{η} and slope spectra $S_{|\nabla\eta|}$, are examined as a function of the radius of the binning region. UAS wave spectra are compared to those of the Spotter wave buoy. UAS slope spectra are compared to slope spectra estimated from Spotter wave spectra and the wavenumber k inferred from the linear dispersion relationship. In section 5, UAS-lidar estimated directional Fourier coefficients are estimated as a function of frequency and compared to those of the Spotter wave buoy. Directional moments derived from the Fourier coefficients are also compared to the Spotter wave buoy. The capability of a UAS with multibeam lidar to estimate wave and slope spectra as well as directional wave quantities is discussed in section 7.

2. Methods

a. Experiment overview

The ROXSI field experiment occurred during July 2022 off China Rock on the Monterey Peninsula, California (Fig. 1). The rocky shore off China Rock has a moderate (1:40) cross-shore slope. In water depths $h < 20$ m, the bathymetry has significant variability, or roughness, at a range of length scales (Fig. 1). A China Rock cross- and alongshore (X, Y) coordinate system is defined where $-X$ is directed toward 285°N. The shoreline has multiple small headlands about 250 m apart with embayments that extend 100 m onshore. During the experiment, a number of instruments, including ADCPs, Spotter wave buoys (Raghukumar et al. 2019), and pressure sensors, were deployed from the shoreline to 30-m water depth (magenta dots in Fig. 1). At eight locations, collocated Spotter wave buoys and time-synchronized pressure sensors were deployed. Spotter wave buoys are GPS-based (Herbers et al. 2012) and are highly effective in capturing wave spectra $S_{\eta}(f)$ and directional moments in the sea-swell ($0.05 < f < 0.3$ Hz) frequency

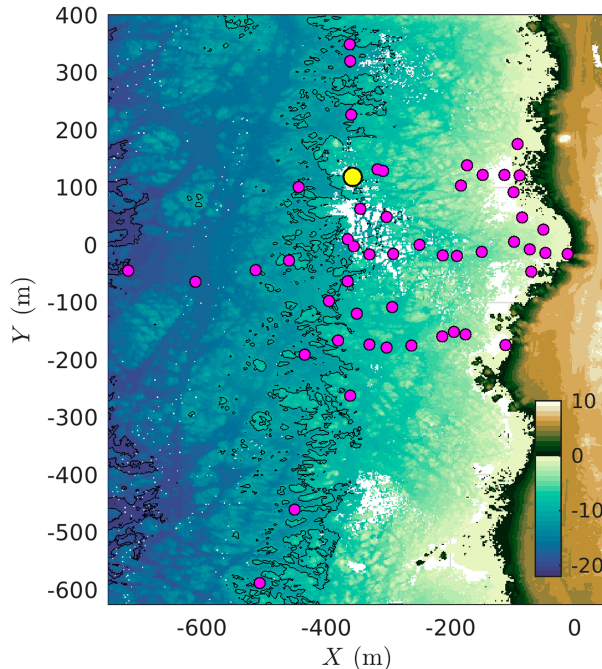


FIG. 1. Bathymetry (z , meters relative to mean sea level) at the China Rock region as a function of local cross-shore X and along-shore Y coordinates. Magenta dots represent all instrument locations. The yellow circle represents the location of the Spotter mooring where the hover took place. Regions in white indicate no bathymetric observations.

band (e.g., Raghukumar et al. 2019; Collins et al. 2024). To estimate directional parameters, wave buoys (whether GPS- or IMU-based) use displacement or slope cross-spectra to estimate the Fourier coefficients of the directional spectra (or directional Fourier coefficients) $a_1(f)$, $a_2(f)$, $b_1(f)$, and $b_2(f)$ (Longuet-Higgins et al. 1963; Kuik et al. 1988). For this study, we calculate spectral quantities from the Spotter wave buoy for the coincident 692-s time period of the UAS hover (described below). Although only tested out to frequencies ≤ 0.3 Hz (Raghukumar et al. 2019; Collins et al. 2024), the Spotter wave buoy reports spectral quantities out to 1 Hz with unknown accuracy from 0.3 to 1 Hz.

b. UAS and lidar package description

We use an eight-rotor Skyfront Perimeter 8¹ as the uncrewed aircraft system (UAS). The Perimeter 8 is powered by a hybrid gasoline–electric propulsion system, consisting of a 32 cc 1-cylinder 2-stroke engine that generates electricity to power the UAS. Two lithium polymer (LiPo) batteries provide startup and emergency backup power. Tip to tip, the Perimeter 8 measures 2.31 m long by 2.2 m wide by 0.37 m high. The Perimeter 8 weighs ≈ 20 kg with 4 L of fuel, and the payload gives it a takeoff weight of ≈ 22.5 kg. With this payload, the UAS was flown for up to 100 min, including takeoff,

kinematic alignment maneuvers, transit, hovers, and landing. The Skyfront Perimeter 8 uses a proprietary PX4-based flight controller and is remotely operated using a 2.4-GHz radio remote controller connected to a Windows laptop running the Skyfront Ground Control Software (GCS) for both manual and automated waypoint flight. The flight controller navigation system was upgraded with an RTK-GNSS module that receives relative position updates from a fixed-location base station onshore. This allows the UAS to maintain its position without drifting over time. With a team of three people, the lidar UAS can be set up and deployed within 30 min of arrival on site. The downtime between each flight to refuel, swap batteries, and resume data collection was approximately 20 min. External LiPo batteries are used for ground power to keep the lidar and GNSS system running without interruption.

The UAS payload is a Phoenix Lidar Systems (PLS) Scout-Ultra,² consisting of a Velodyne Ultra Puck (VLP-32C) lidar, a proprietary PLS NavBox, and a 24-MP Sony A6K-Lite RGB camera. The Scout-Ultra NavBox integrates the IMU, GNSS receiver, data storage, CPU, Wi-Fi telemetry, power supply, and I/O components necessary for collecting survey-grade data. The GNSS receiver is a Novatel OEM7720, and the IMU is an Inertial Laboratories IMU-P. Dual helical GNSS antennas are mounted onto opposing UAS motor arms with 1.54-m separation, enabling accurate heading solutions. The IMU and dual GNSS data are postprocessed using Novatel Inertial Explorer version 8.90 software to produce a trajectory file for determining sensor position and orientation. The Scout-Ultra is controlled separately from the UAS via a Wi-Fi link to a second Windows laptop running Phoenix Lidar Systems' Spatial Explorer version 6.0.7. The PLS software displays real-time point cloud, image preview, and payload telemetry data and allows for remote activation of the lidar and camera sensors. RGB camera images were taken at 1 Hz.

The Velodyne Ultra Puck lidar was originally developed for the automobile industry and has been adapted for surveying and robotics applications. Although it is slightly less accurate than fixed-location lidars (3 vs 0.75 cm accuracy) previously used in surfzone studies (Brodie et al. 2015), its low cost, low power, multibeam scan pattern, long range, small form factor, and lightweight (1 kg) make it well suited for this UAS application. The lidar uses a 903-nm laser, which performs better on water surfaces than 1550-nm lasers (Wojtanowski et al. 2014; Fiedler et al. 2021). The 32 beams scan over 360°, on an axis 90° from the nose of the UAS. The beams are organized in a nonlinear distribution, with most beams concentrated in the center of the vertical field of view, where data resolution is increased, resulting in a 40° off-axis field of view (from -25° to $+15^\circ$). The pulse repetition rate of the sensor is 600 000 measurements per second (600 kHz). The programmable frame rate of the lidar ranges from 5 to 20 Hz. Similar to Feddersen et al. (2023), we used 10 Hz (600 RPM, ± 3 RPM), which gives a horizontal angular (azimuthal) resolution of 0.2° . At the 10-Hz frame rate and sampling a 90° region below the UAS results in 0.025-s time uncertainty of a return, which is insignificant for the analysis

¹ <https://skyfront.com/perimeter-8>.

² <https://phoenixlidar.com/>.

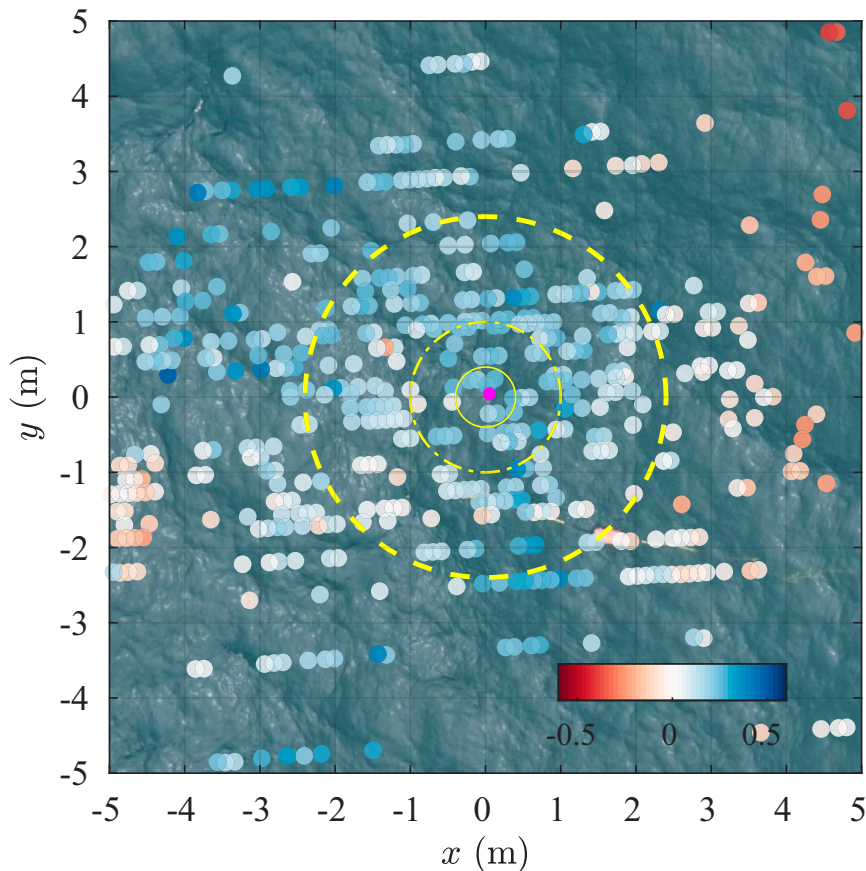


FIG. 2. Georectified sea surface image in offset China Rock (x, y) coordinates with overlaid lidar-based sea surface elevation $\eta(x, y)$ (colored dots) at that specific time. The magenta dot indicates the instantaneous UAS location, which is offset slightly from the time-averaged UAS location. The solid, dash-dot, and dashed yellow circles represent radii of $R = \{0.4, 1, 2.4\}$ m around $(x, y) = (0, 0)$ m. The time is 1459:08 PDT 19 Jul 2022.

on surface gravity wave time scales > 1 s. The maximum measurement range is 200 m with a ± 3 -cm range accuracy. Laser beam divergence is 3.43 mrad on the horizontal axis (cross-shore) and 1.72 mrad on the vertical axis (alongshore), resulting in a $12.5 \text{ cm} \times 6.6 \text{ cm}$ footprint of an individual lidar return directly below the scanner when hovering at 33 m above the sea surface. The Velodyne Ultra Puck does not provide usable metrics to evaluate the quality of a return. The lidar returns are transformed into earth coordinates in Spatial Explorer software using the postprocessed position and orientation data. The resulting point cloud was exported to a LAS format file. Lidar returns were quality-controlled to remove points closer than 8 m or farther than 100 m from the lidar.

c. Hover near the spotter wave buoy

Most missions had the UAS hovering sequentially over locations of pressure sensors located mostly in the surfzone of the rocky shoreline for approximately 10 min at a time for flights of 80–100-min duration. However, we performed one mission where the UAS hovered near the location of a Spotter wave buoy (Fig. 1, yellow circle), approximately 250 m from the

mean shoreline. This hover occurred on 19 July 2022, started at 1458:12 PDT, and lasted for 692 s. At this time, the Spotter significant wave height integrated from 0.04 to 0.4 Hz was $H_s = 1.17$ m with an energy-weighted mean period of $\bar{T} = 6.1$ s. During the morning, the wind (measured 300 m offshore at 4 m above the sea surface) had been 6 m s^{-1} blowing onshore ($+x$ direction). However, during the hover, the wind was weaker at 2.5 m s^{-1} onshore. The UAS was hovering at 33-m elevation relative to the sea surface where the wind was likely stronger than measured.

The hovering UAS was oriented with the nose pointing in the alongshore $+Y$ direction, so the lidar was oriented for cross-shore scanning. The latitude and longitude of lidar returns are converted to the UTM-based local China Rock (X, Y) coordinates. The vertical locations of the lidar returns are in NAVD88 and are demeaned to represent sea surface elevation. The 2-Hz sampled locations of the UAS reveal that the UAS maintained a nearly constant hovering position. The UAS position x standard deviation $\sigma_x = 0.055$ m is small as is the y standard deviation $\sigma_y = 0.084$ m, with maximum position deviation < 0.2 m in x and y . During the hover, the UAS held its orientation consistently with a heading standard

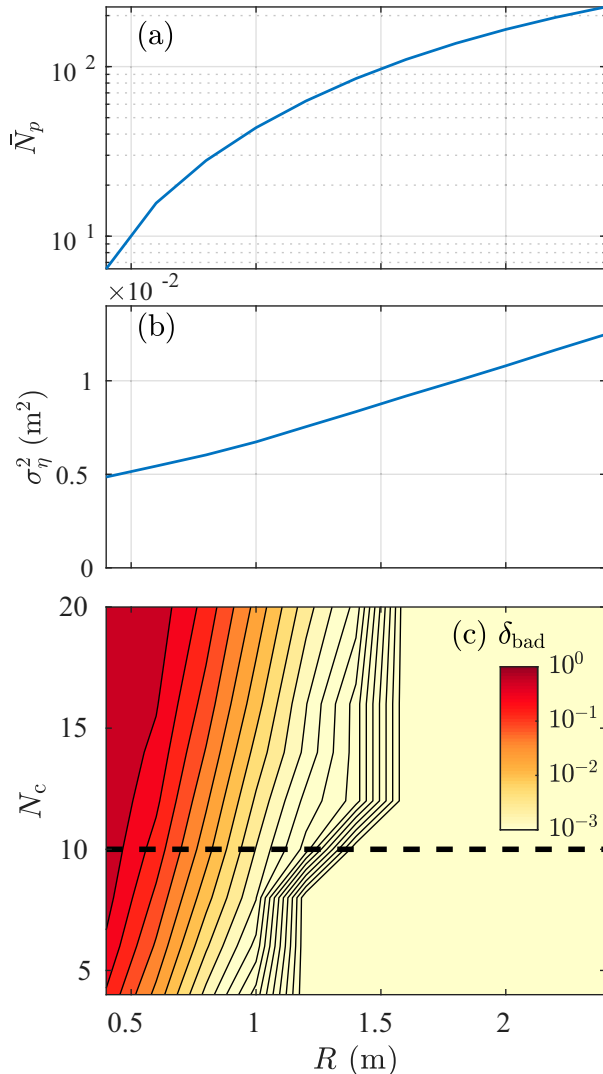


FIG. 3. Lidar return statistics within the sample region vs radius R . (a) The time-averaged number of returns within the sample region \bar{N}_p . (b) The mean variance of the sea surface returns within the sample region σ_η^2 [(1)]. (c) The δ_{bad} (fraction of time that the return number is below N_c) as a function of the return cutoff number N_c and the radius R . The contour kinks reflect the discrete sampling of R and N_c . The black-dashed line represents $N_c = 10$.

deviation of 0.3° , a pitch standard deviation of 0.7° , and a roll standard deviation of 0.5° . The mean pitch was 0.8° and the mean roll was 2.7° allowing the UAS to maintain position in the wind for this hover. Stronger winds likely result in larger position and heading, pitch, and roll variability.

An example of a single 10-Hz lidar snapshot is shown in Fig. 2. We define a local coordinate system $x = X - \bar{X}$ where (\bar{X}, \bar{Y}) are the mean location of the UAS during the hover. From the georectified image, a rough but not whitening sea surface is visible with short wavelengths ≈ 1 m that ride on top of the longer sea and swell. The Velodyne Ultra lidar beams are largely oriented along the $\pm x$ direction, also approximately the direction of wave propagation, and lidar returns are largely

concentrated at $|y| \leq 2$ m. The number of lidar returns at this offshore location was significantly less than farther onshore due to the lack of breaking waves and increased water clarity at this cross-shore location (divers reported 6-m visibility 2 days later). Lidar returns indicate that the sea surface η varies spatially at ± 0.5 m at a range of scales.

3. Lidar data processing and return statistics

We define a *sampling region* as a circle of radius R centered on the mean hover location $(x, y) = (0, 0)$ m. A circle is chosen so as to not bias directional estimates; i.e., all directions have the same sampling region width. We estimate lidar return statistics and sea surface elevation and slopes as a function of R , which varies from 0.4 to 2.4 m in 0.2-m increments. An example of sampling regions is shown in Fig. 2 with radii of $R = \{0.4, 1, 2.4\}$ m. The number of lidar returns within a sampling region, defined as $N_p(t; R)$, is higher for larger R (Fig. 2). We define two types of averaging. The first is averaging over the lidar returns within the sample region, denoted by $\langle \dots \rangle$. The second is a time average over the 692 s of the UAS hover, denoted by an overbar. Thus, $\langle \bar{\eta} \rangle$ is equal to zero.

The time-averaged number of lidar returns $\bar{N}_p(R)$ varies from six points for $R = 0.4$ m and increases quadratically to $\bar{N}_p = 225$ for $R = 2.4$ m (Fig. 3a). The ratio \bar{N}_p/R^2 is roughly constant at $\approx 40 \text{ m}^{-2}$, indicating that the lidar return density is uniform across the R range (0.4–2.4 m). At larger R , this ratio decreases due to the lidar beam distribution, and $R > 2.4$ m is thus not considered.

We estimate the time-averaged vertical variance of lidar returns within a sample region $\sigma_\eta^2(R)$ as

$$\sigma_\eta^2(R) = \langle \overline{\eta'^2} \rangle, \quad (1)$$

where $\eta'_i(t) = \eta_i(t) - \langle \eta(t) \rangle$. Thus, σ_η^2 represents a combination of instrument noise and the true sea surface variability. The mean return vertical variance $\sigma_\eta^2(R)$ varies in a weakly quadratically manner from 0.005 m^2 at $R = 0.4$ m to 0.013 m^2 at $R = 2.4$ m (Fig. 3b). Quadratic σ_η^2 variation is consistent with the sea surface primarily being a plane, whereas random and independent instrument noise would lead to a $\sigma_\eta^2(R)$ constant with R . Extrapolating the curve to $R = 0$ yields an instrument (lidar plus orientation/position) η noise variance estimate of 0.0035 m^2 or 0.06 m. The quoted Velodyne Ultra Puck accuracy is 0.03 m, or half of the inferred η noise standard deviation, suggesting the remainder is due to UAS orientation and position uncertainty. The UAS orientation and position uncertainty will be affected by variables such as GNSS quality and IMU hardware. That the η noise standard deviation is so small relative to the expected wave amplitude gives confidence in the results.

For a particular time, a minimum number of lidar returns above a cutoff N_c are required [i.e., $N_p(t) > N_c$] to estimate sea surface parameters (see below); otherwise, interpolation over that time is required. We define the fraction of time that data are bad $\delta_{\text{bad}}(R, N_c)$ as the fraction of time that $N_p(t; R) < N_c$. Small δ_{bad} results in minimal time series interpolation prior to estimating wave statistics, and the smaller N_c yields smaller δ_{bad} and less interpolation. Yet small N_c may lead to noisy estimates

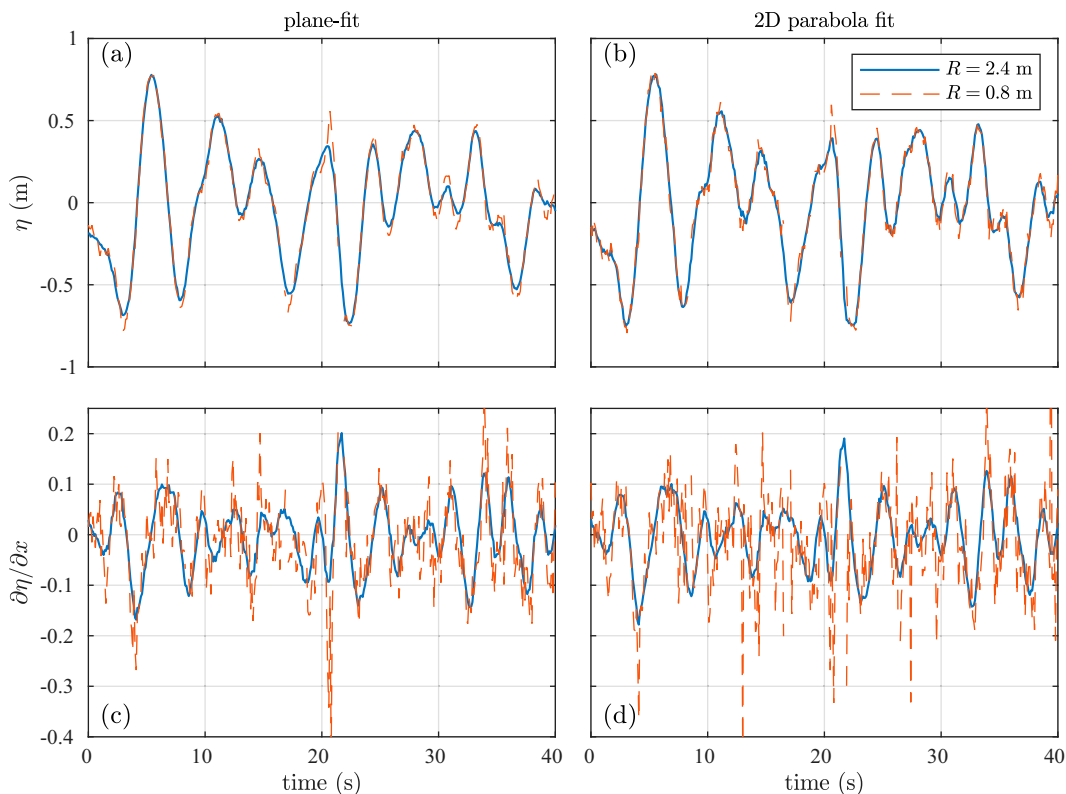


FIG. 4. Time series of (a),(b) η and (c),(d) $\partial\eta/\partial x$ for $R = 2.4$ m (blue) and $R = 0.8$ m (orange-dashed) and $N_c = 10$. (left) The plane-fit and (right) the 2D parabola-fit.

of η and its slope. To determine what N_c to choose, we examine the statistics of δ_{bad} as a function of R and N_c varying from $N_c = 4$ to $N_c = 20$. For $R > 1.2$ m, the fraction of bad data $\delta_{\text{bad}}(R, N_c)$ is largely independent of N_c (contour lines in Fig. 3c are largely vertical) and $\delta_{\text{bad}} < 10^{-3}$ for all N_c . For smaller $R \leq 0.6$ m, δ_{bad} is always > 0.05 and grows rapidly with N_c . Thus, we do not consider further $R \leq 0.6$ m. As δ_{bad} only weakly depends on N_c for $R \geq 0.8$ m, we choose an intermediate $N_c = 10$ for further analysis, resulting in a $\delta_{\text{bad}} < 0.013$ for $R \geq 0.8$ m, resulting in minimum interpolation requirement.

To calculate wave spectra and directional moments, time series of η , $\partial\eta/\partial x$, and $\partial\eta/\partial y$ at $(x, y) = (0, 0)$ m are required. We estimate these parameters using two different least squares fits: 1) a plane-fit and 2) a 2D parabola-fit, which are based on a first- or second-order Taylor series expansion of the sea surface around $(x, y) = (0, 0)$ m, consistent with the σ_η^2 variation largely being a plane (Fig. 3b). The fit parameters are estimated over a range of R for times when $N_c \geq 10$. The plane-fit fits a plane to the available lidar returns in the sampling region, i.e.,

$$\eta_i(t, x_i, y_i) = \frac{\partial\eta}{\partial x}(t)x_i + \frac{\partial\eta}{\partial y}(t)y_i + \eta(t), \quad (2)$$

where (x_i, y_i) and η_i are the observed horizontal position and sea surface elevation of the lidar returns (Fig. 2), and there are three fit parameters (η , $\partial\eta/\partial x$, and $\partial\eta/\partial y$). The 2D parabola-fit fits to a 2D parabola, i.e.,

$$\eta_i(t, x_i, y_i) = \frac{1}{2}\frac{\partial^2\eta}{\partial x^2}(t)x_i^2 + \frac{1}{2}\frac{\partial^2\eta}{\partial y^2}(t)y_i^2 + \frac{\partial^2\eta}{\partial y\partial x}(t)x_i y_i + \frac{\partial\eta}{\partial x}(t)x_i + \frac{\partial\eta}{\partial y}(t)y_i + \eta(t), \quad (3)$$

and has three additional fit parameters $\partial^2\eta/\partial x^2$, $\partial^2\eta/\partial y^2$, and $\partial^2\eta/\partial x\partial y$. Both fits are performed for all times where $N_p > N_c$ at all $R \geq 0.8$ m. Any times with $N_p < N_c$ lidar returns are linearly interpolated in time. Based on the time-averaged mean-square fit error and the $\sigma_\eta^2(R)$, the overall (time-averaged) fit skill is > 0.94 for all $R \geq 0.8$ and both methods. At occasional times, the fit skill can be reduced, but using fit skill to remove parameter estimates had no effect on the results and is not performed here.

The advantage of the plane-fit [(2)] is that, with fewer fit parameters, their estimates should be more stable. The disadvantage is that, for a wavelength λ , an R significantly shorter than λ is required to resolve the wave. This places an upper-frequency limit, through the surface gravity wave dispersion relationship [(A1)], on the estimated parameters. As λ gets smaller (frequency increases), we expect the spectral levels to decrease with larger R , as the fit essentially acts as a low-pass filter. The 2D parabola-fit [(3)] has more fit parameters, which will have more noise than that of the plane-fit. However, by including quadratic terms at a fixed R , a shorter λ should be resolvable relative to the plane-fit,

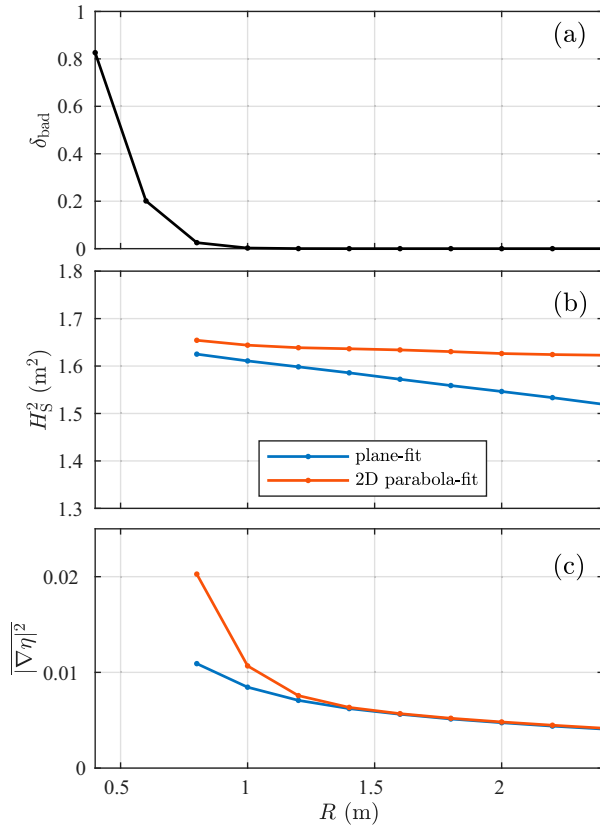


FIG. 5. (a) Fraction of time with bad data δ_{bad} , (b) squared significant wave height H_s^2 [(4)], and (c) mean-square surface slope $|\nabla\eta|^2$ [(5)] vs radius R all for $N_c = 10$. In (b) and (c), the blue and orange lines represent the plane-fit and 2D parabola-fit, respectively.

thereby increasing the resolved frequencies. Throughout, we will explore the relative merits of both fit methods. At larger λ , other challenges are present that depend on R . The wave slope scales as wave amplitude over wavelength a/λ , and thus, these smaller slopes will be harder to robustly estimate.

4. Lidar observations of sea surface and slope

a. Time series of η and $\partial\eta/\partial x$

Short, 40-s, time series of the plane-fit and 2D parabola-fit η and $\partial\eta/\partial x$ for two radii are shown in Fig. 4 to illustrate the effects of varying R and the fit method. Recall $N_c = 10$ is fixed. The plane-fit η with $R = 2.4$ m varies ± 0.5 m with evident variability over 3–8-s periods (Fig. 4a, blue curve). The $R = 0.8$ m plane-fit η varies similarly but has more high-frequency variability (orange-dashed in Fig. 4a). The 2D parabola-fit η for $R = 2.4$ m (Fig. 4b, blue curve) is quite similar to that of the plane-fit, and the η for $R = 0.8$ m also has more high-frequency variability with some minor differences relative to the plane-fit η . The differences in $\partial\eta/\partial x$ for the two radii are much starker (Figs. 4c,d) than those for η . The plane-fit $\partial\eta/\partial x$ for $R = 2.4$ m has a smooth curve (Fig. 4c) with variability at time scales similar to η with

magnitude ≈ 0.1 , indicating weak nonlinearity. However, the $R = 0.8$ m plane-fit η has significantly more high-frequency variability than for $R = 2.4$ m. The 2D parabola-fit $\partial\eta/\partial x$ for $R = 2.4$ m (blue curve in Fig. 4d) is similar to the plane-fit. However, the 2D parabola-fit with $R = 0.8$ m $\partial\eta/\partial x$ has even more high-frequency variability than for the plane-fit. For both η and $\partial\eta/\partial x$, the greater stability and low-pass filtering effect of increasing R are evident. The pattern with $\partial\eta/\partial y$ is similar (not shown).

b. Time-averaged sea surface and slope statistics

To evaluate the η , $\partial\eta/\partial x$, and $\partial\eta/\partial y$ from the two fit methods, we examine two bulk statistics, squared significant wave height H_s^2 and mean-square wave slope as a function of R . Significant wave height H_s is defined in a standard manner through sea surface elevation variance:

$$H_s = 4 \overline{\eta^2}^{1/2}. \quad (4)$$

Note this definition includes all frequencies up to the Nyquist frequency of 5 Hz in the estimate of H_s . The mean-square wave slope $|\nabla\eta|^2$ is

$$\overline{\left(\frac{\partial\eta}{\partial x}\right)^2 + \left(\frac{\partial\eta}{\partial y}\right)^2}. \quad (5)$$

For $R = 0.4$ m and $R = 0.6$ m, $\delta_{\text{bad}} = 0.83$ and $\delta_{\text{bad}} = 0.2$, respectively (Fig. 5a). With so many bad data points, further statistics are not calculated or examined for $R \leq 0.6$ m. For $R = 0.8$ m, $\delta_{\text{bad}} = 0.03$, and for larger R , the δ_{bad} is effectively zero. Thus, we examine statistics for $R \geq 0.8$ m only. The plane-fit H_s^2 slowly decreases from 1.63 m^2 at $R = 0.8$ m to 1.52 m^2 at $R = 2.4$ m (Fig. 5b). This decrease is consistent with the larger R , providing more statistical stability and acting as a low-pass filter. Relative to the plane-fit, the 2D parabola-fit H_s^2 is relatively constant with R only decreasing slightly from 1.65 to 1.62 m^2 over the R range. This indicates that for this R range, the 2D parabola-fit with its extra fit parameters reduces the low-pass filter effect. For the plane-fit, the mean-square slope $|\nabla\eta|^2$ decreases steadily from 0.011 at $R = 0.8$ m to 0.0041 at $R = 2.4$ m (Fig. 5c). For the 2D parabola-fit, $|\nabla\eta|^2$ is twice as large as for the plane-fit for $R = 0.8$, consistent with the $\partial\eta/\partial x$ time series (Fig. 4d). However, for $R \geq 1.2$ m, the 2D parabola-fit $|\nabla\eta|^2$ is similar to that of the plane-fit method (Fig. 5c). The decay with R suggests that slope is more sensitive to R than η is for the 2D parabola-fit method.

c. Spectra of sea surface elevation and slope

Sea surface elevation spectra $S_\eta(f)$ are estimated for both fit methods with 24 degrees of freedom (DOF) and frequency resolution of ≈ 0.01 Hz. Slope spectra $S_{|\nabla\eta|}(f)$ are also estimated from the spectra of $\partial\eta/\partial x$ and $\partial\eta/\partial y$:

$$S_{|\nabla\eta|}(f) = S_{\eta_x}(f) + S_{\eta_y}(f). \quad (6)$$

We examine UAS-lidar wave spectra $S_\eta(f)$ dependence on radius R for both fit methods and compare it to the wave spectra

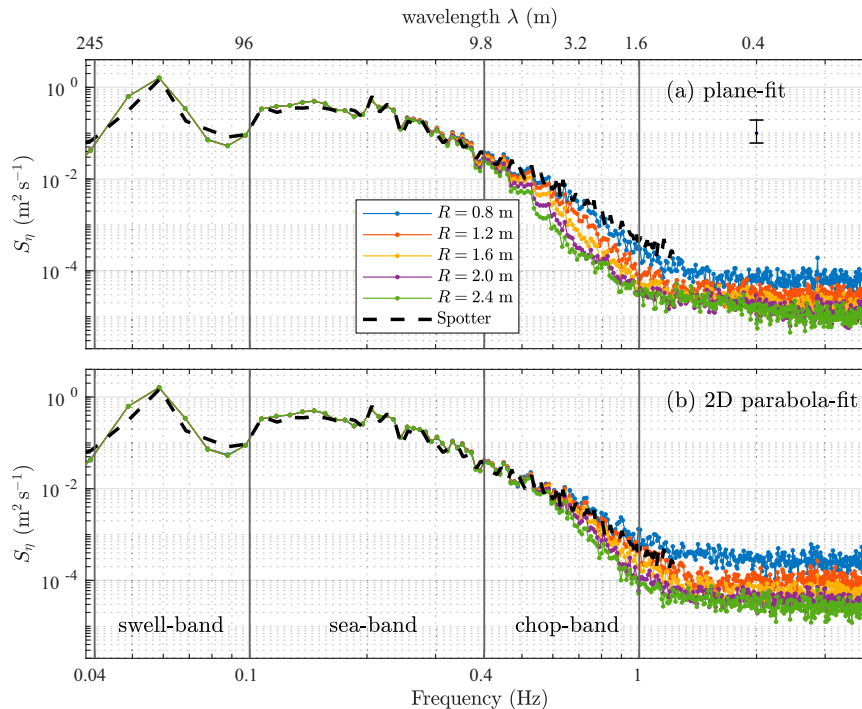


FIG. 6. UAS-lidar sea surface elevation spectra $S_{\eta}(f)$ vs frequency for the (a) plane-fit and (b) 2D parabola-fit methods for $R = \{0.8, 1.2, 1.6, 2.0, 2.4\}$ m. The black-dashed curve is the Spotter wave buoy spectrum over the same time period (shown out to 1 Hz). The black error bar indicates the 95% spectra confidence limits at 24 DOF for both lidar- and wave buoy-based spectra. On the top is shown the wavelength λ associated with select f through the linear surface gravity wave dispersion relationship [(A1)] at a depth of 10 m. The gray vertical lines demarcate the swell, sea, and chop frequency bands as indicated in (b).

from the collocated Spotter wave buoy (Fig. 6). Hereafter, we define three specific frequency bands. First, the swell band spans $0.04 \leq f < 0.1$ Hz. The sea band spans $0.1 \leq f < 0.4$ Hz. We also define a “chop” band as $0.4 \leq f < 1$ Hz band. The plane-fit $S_{\eta}(f)$ for $R \geq 0.8$ m matches well the Spotter wave spectra across the $0.04 < f < 0.4$ Hz band that encompasses the swell and sea bands. In this band, the plane-fit and 2D parabola-fit $S_{\eta}(f)$ are nearly similar for all $R \geq 0.8$ m. At this location and depth, a frequency of 0.4 Hz corresponds to a wavelength of $\lambda \approx 10$ m, with ratio R/λ being less than 0.25 for all R , indicating that the fit methods should be robust. At frequencies > 0.4 Hz, $S_{\eta}(f)$ decreases more rapidly for larger R , consistent with the low-pass filter effect with larger R , and at 0.6 Hz, significant $S_{\eta}(f)$ differences with R are evident, particularly for the plane-fit (Fig. 6). The 2D parabola-fit $S_{\eta}(f)$ has less spectral variation with R in the “chop” (0.4–1 Hz) band and then the plane-fit consistent with the H_s^2 changes with R for both methods (Fig. 5b). This is likely a result of the 2D parabola-fit being able to resolve shorter wavelengths at a particular R . For both methods, the spectral noise floor [i.e., flat $S_{\eta}(f)$] occurs at $f > 1$ Hz, corresponding to a wavelength λ of 1.6 m, with levels that decrease with R . At $f = 1$ Hz, the ratio of R/λ varies from 0.5 to 1.5. At the larger R/λ values, the fit method will act as a low-pass filter, as observed in Fig. 6. The noise floor depends on method and R , but for

$R \geq 1.2$ m, the noise floor is $< 10^{-4} \text{ m}^2 \text{ s}^{-1}$. Overall, either method will work well for estimating wave spectra in the sea-swell (0.04–0.4 Hz) band.

We next examine the effect of R on slope spectra $S_{|\nabla\eta|}(f)$ [(6)] for both the plane-fit and 2D parabola-fit methods (Fig. 7). The Spotter does not report wave slope, and thus, a direct comparison cannot be made. However, from the Spotter wave spectra, we can estimate slope spectra as $k^2(f)S_{\eta}(f)$, where k is estimated from the linear dispersion relationship [(A1)] at each frequency at a depth of 10 m. In the swell band ($f < 0.1$ Hz), the plane-fit and 2D parabola-fit $S_{|\nabla\eta|}(f)$ for $R = 0.8$ m are elevated, indicating noise contamination. In this band, the $S_{|\nabla\eta|}(f)$ converges with larger R (Fig. 7), suggesting that for $R \geq 1.2$ m, the slope spectra are well estimated. In addition, in the swell band, the Spotter inferred $k^2S_{\eta}(f)$ (black-dashed in Fig. 7) matches well the slope spectra for $R \geq 1.6$ m, further suggesting $S_{|\nabla\eta|}(f)$ is well estimated in this band. For $R \geq 1.6$ m, the equivalent swell-band wave slope $(ak)_{\text{swell}} = 0.0085$ [(A2)], corresponding to an angle of 0.49° , is very small.

In the $0.1 < f < 0.4$ Hz sea band, the spectra are similar for both methods for all $R > 0.8$ m. Consistent with this, the equivalent sea-band wave slopes $(ak)_{\text{sea}}$ [(A2)] are similar in this band varying from 0.076 to 0.072. In addition, the inferred Spotter $k^2S_{\eta}(f)$ matches well the slope spectra, which all

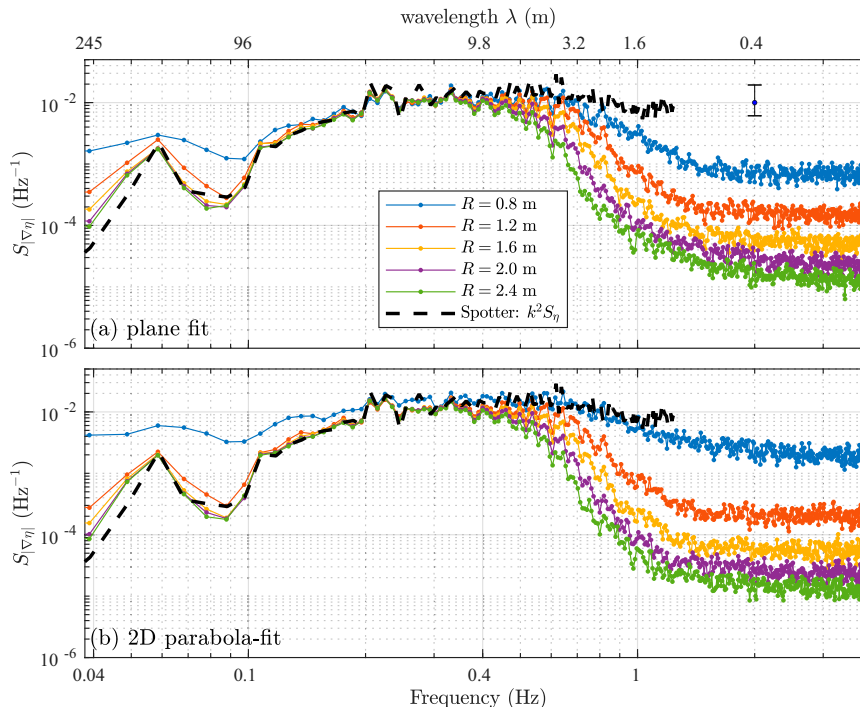


FIG. 7. UAS-lidar sea surface elevation slope spectra $S_{|\nabla\eta|}$ [(6)] vs frequency for the (a) plane-fit and (b) 2D parabola-fit methods for $R = \{0.8, 1.2, 1.6, 2.0, 2.4\}$ m. The black-dashed curve is the Spotter estimated slope spectrum $k^2 S_{\eta}(f)$ using the dispersion relationship [(A1)] and a depth of 10 m. The black error bar indicates the 95% spectra confidence limits at 24 DOF for the lidar-based spectra. On the top is shown the wavelength λ associated with select f through the linear surface gravity wave dispersion relationship at a depth of 10 m.

together suggests that slope spectra are well estimated in this band. At higher frequencies ($f > 0.4$ Hz), the $S_{|\nabla\eta|}(f)$, separate as a function of R , is consistent with the reduced $|\nabla\eta|^2$ with R (Fig. 5c) and the low-pass filter interpretation. Generally at $f > 2$ Hz for both methods, a noise floor is reached, whose level is lower for larger R , also consistent with the low-pass filter interpretation. For both methods, at $R = 0.8$, the $S_{|\nabla\eta|}(f)$ has a peak near $f = 0.6$ Hz which only weakly decays out to 1 Hz, whereas the slope spectra for larger R fall off much more rapidly. In the “chop” band ($0.4 < f < 1$ Hz), the equivalent ak is similar to that in the sea band and varies from 0.1 to 0.05 for $R = 0.8$ m to $R = 2.4$ m, consistent with Fig. 7. The Spotter inferred slope spectra $k^2 S_{\eta}(f)$ match very well the $R = 0.8$ m 2D parabola-fit $S_{|\nabla\eta|}(f)$ in this band, suggesting that the slope of waves with wavelength as small as 1.6 m may be well estimated with the parabola-fit. Similar to $|\nabla\eta|^2$ and H_s^2 (Figs. 5b,c), slope spectra $S_{|\nabla\eta|}(f)$ are more sensitive to R than $S_{\eta}(f)$ particularly at lower and higher frequencies. Overall, the results suggest that for $R \geq 1.2$ m, the slope spectra are well estimated at $f < 0.4$ Hz.

5. Directional Fourier coefficients and directional moments

Wave-directional Fourier coefficients depend not only on the spectra of η , $\partial\eta/\partial x$, and $\partial\eta/\partial y$ but also on their cross-spectra

(Longuet-Higgins et al. 1963). Here, we estimate the directional Fourier coefficients $[a_1(f), b_1(f), a_2(f), b_2(f)]$ from the UAS-lidar derived spectra and cross-spectra using standard methods (appendix) for $R \geq 1.2$ m and both fit methods (Fig. 8). The plane-fit $a_1(f)$ follows the Spotter $a_1(f)$ for $R \geq 2$ m in the swell band ($0.04 < f < 0.1$ Hz). Most of the mismatch occurs near 0.08–0.09 Hz, where the S_{η} and slope spectra levels are reduced (Figs. 6 and 7). The plane-fit $a_1(f)$ matches the Spotter $a_1(f)$ in the sea band ($0.1 < f < 0.4$ Hz) for all R (Fig. 8a). The 2D parabola-fit $a_1(f)$ is overall similar but is closer to the Spotter $a_1(f)$ in the swell band for the largest R (Fig. 8b). Overall, $b_1(f)$, $a_2(f)$, and $b_2(f)$ also agree well with the Spotter in the sea band ($0.1 < f < 0.4$ Hz) for the range of R (Figs. 8c–h) for both methods. For both methods, $b_1(f)$ and $b_2(f)$ match the Spotter’s estimate in the swell band for larger R (Figs. 8c,d,g,h). However, for $a_2(f)$, the comparison is poor in the swell band (Figs. 8e,f). The Spotter $a_2(f)$ is quasi-constant in the swell band. For smaller R , the $a_2(f)$ for both methods varies strongly across the swell band but becomes more constant at larger R , albeit at a lower value than the Spotter.

The preceding comparison between estimated directional Fourier coefficients and those of the Spotter is qualitative. Here, we make the comparison quantitative with an unweighted mean-square error metric defined as

$$\epsilon_{a_1} = \{[a_1(f) - a_1^{\text{SP}}(f)]^2\}, \quad (7)$$

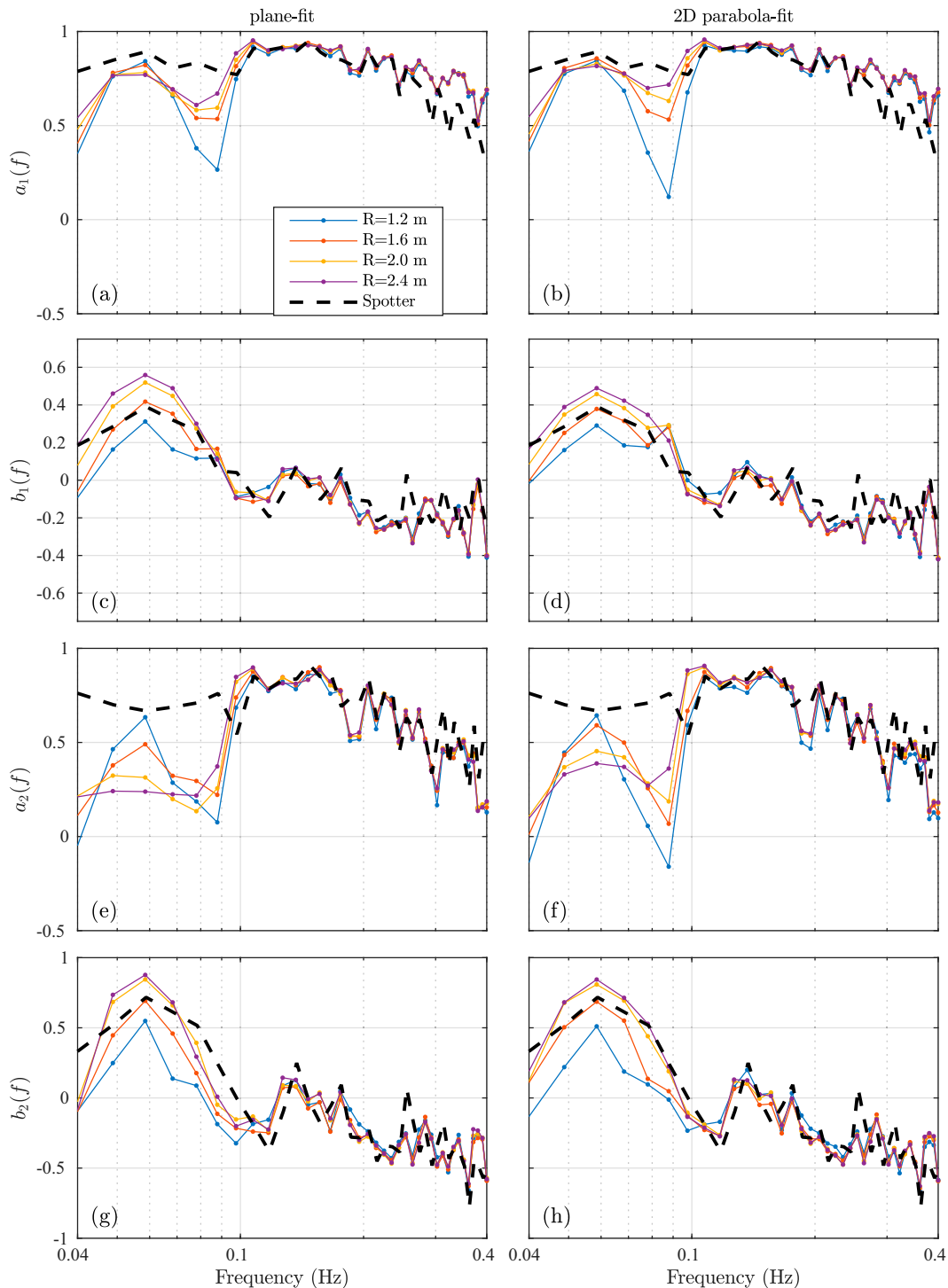


FIG. 8. Directional moments (a),(b) $a_1(f)$, (c),(d) $b_1(f)$, (e),(f) $a_2(f)$, and (g),(h) $b_2(f)$ vs frequency for (left) plane-fits and (right) 2D parabola-fits for five different sampling region radii of $R = \{1.2, 1.6, 2.0, 2.4\}$ m. The dashed line is the Spotter wave-buoy-derived directional moments. Note that we limit comparison to 0.04–0.4 Hz.

where the $\{\dots\}$ represents an average over the frequency band 0.04–0.25 Hz and a_1^{Sp} is a_1 from the Spotter. This seaswell frequency band contains the bulk of the wave energy (Fig. 6) and also is the range where the Spotter has been

validated (Raghukumar et al. 2019). The errors for the other directional Fourier coefficients ϵ_{b_1} , ϵ_{a_2} , and ϵ_{b_2} are similarly defined. These errors are estimated for both plane-fit and 2D parabola-fit methods. Consistent with Figs. 8a and 8b, the

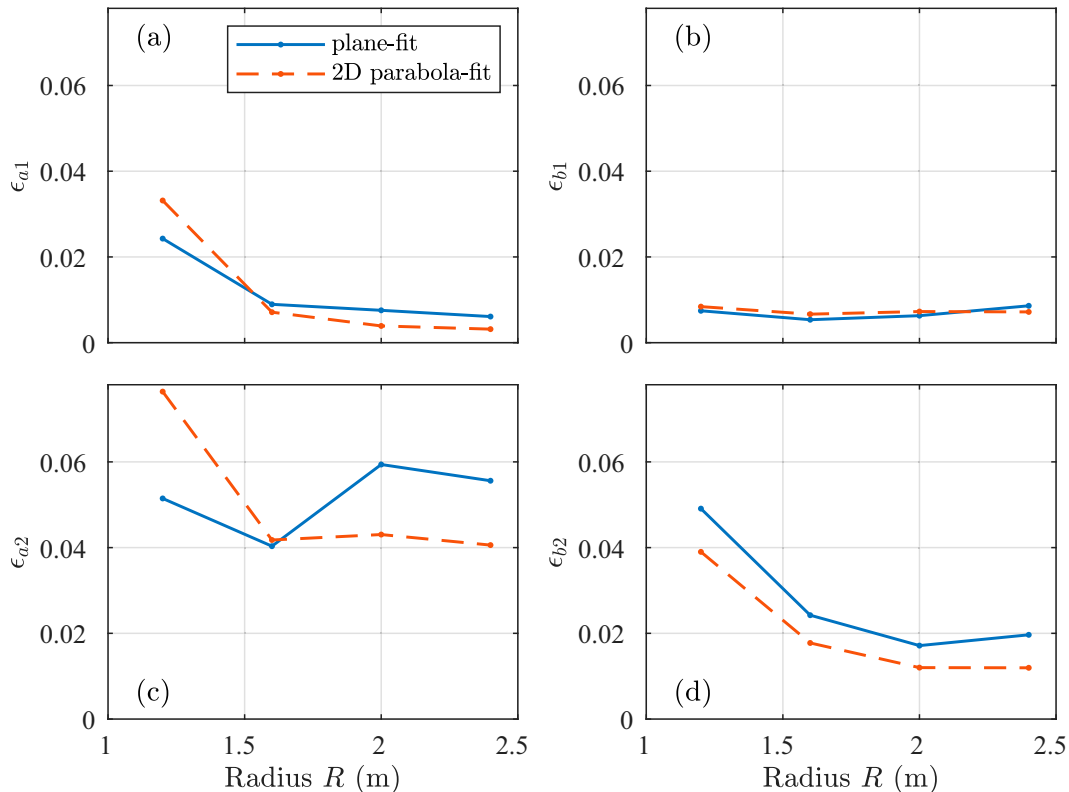


FIG. 9. Directional Fourier coefficient errors vs radius R for (a) ϵ_{a1} , (b) ϵ_{b1} , (c) ϵ_{a2} , and (d) ϵ_{b2} based on (7). The solid curve is from the plane-fit, and the dashed is from the 2D parabola-fit. [The error metric (7)] is integrated over the frequency band from 0.04 to 0.25 Hz containing the majority of wave energy and where the Spotter has been validated.

mean-square error ϵ_{a1} decreases with increasing R with smallest error $\epsilon_{a1} \approx 0.005$ at $R = 2.4$ m (Fig. 9a), which is a small error relative to the $a_1(f)$ variability (Fig. 8a). The 2D parabola-fit method has slightly lower ϵ_{a1} than the plane-fit method. For $b_1(f)$, ϵ_{b1} is small for all R and largely decreases with R , and the 2D parabola-fit method is marginally better than the plane-fit (Fig. 9b). Consistent with Figs. 8e and 8f, the ϵ_{a2} has the largest error of all directional Fourier coefficients (Fig. 9c). For the 2D parabola-fit, ϵ_{a2} decreases or plateaus with R , whereas the plane-fit ϵ_{a2} is not monotonic, and for $R \geq 2$ m, the 2D parabola-fit ϵ_{a2} is substantially larger than that of the plane-fit. For $b_2(f)$, the error ϵ_{b2} is large for small R and largely decreases with R (Fig. 9d). As with other directional Fourier coefficients, the 2D parabola-fit has smaller ϵ_{b2} than the plane-fit and at $R = 2.4$ is at levels similar to ϵ_{a1} . Note that an energy-weighted error metric gives similar results as (7).

Accurately estimating directional Fourier coefficients is essential for any directional wave measurement, whether wave buoy or remote sensing. However, interpreting these directional Fourier coefficients can be opaque. For practical interpretation of directional wave properties, the directional Fourier coefficients are used to estimate directional moments such as the mean wave angle $\theta(f)$ and a directional spread $\sigma_\theta(f)$ at each frequency (Kuik et al. 1988, also see the appendix). Alternatively, they are used as inputs for directional spectra estimators

such as MEM or IMLE (e.g., Oltman-Shay and Guza 1984). Mean wave direction has two definitions $\theta_1(f)$ [(A7)] and $\theta_2(f)$ [(A8)] which use (a_1, b_1) and (a_2, b_2) , respectively (Kuik et al. 1988). The mean wave angle is defined as the direction of wave propagation in the China Rock coordinate system. Thus, on-shore propagating waves with a component in the $+y$ direction have positive θ and with a component in the $-y$ direction have negative θ . Similarly, wave directional spread has two definitions (Kuik et al. 1988): the first $\sigma_\theta(f)$ [(A9)] utilizing (a_1, b_1) only and $\sigma_\theta^*(f)$ utilizing all directional Fourier coefficients [(A10)]. We estimate directional moments across the swell and sea bands for both fit methods at $R = 2.4$ m, which resulted in the smallest directional Fourier coefficient error. The $R = 2.4$ m corresponds to $R/\lambda = 0.24$ at the highest sea-band frequency ($f = 0.4$ Hz), indicating that the low-pass filter effect is still weak.

For the two methods, the $\theta_1(f)$ varies from $\approx 25^\circ$ to 0° in the swell band and, in the sea band, is largely negative and reducing with frequency. The $\theta_1(f)$ from the two methods largely agrees well with the Spotter (Fig. 10a), consistent with the well-estimated $a_1(f)$ and $b_1(f)$ (Figs. 8 and 9). The largest $\theta_1(f)$ differences between the two methods and Spotter wave buoy occur in the swell band with differences as large as 13° for the plane-fit method. Using energy-weighted directional Fourier coefficients (appendix), the 2D parabola-fit swell band

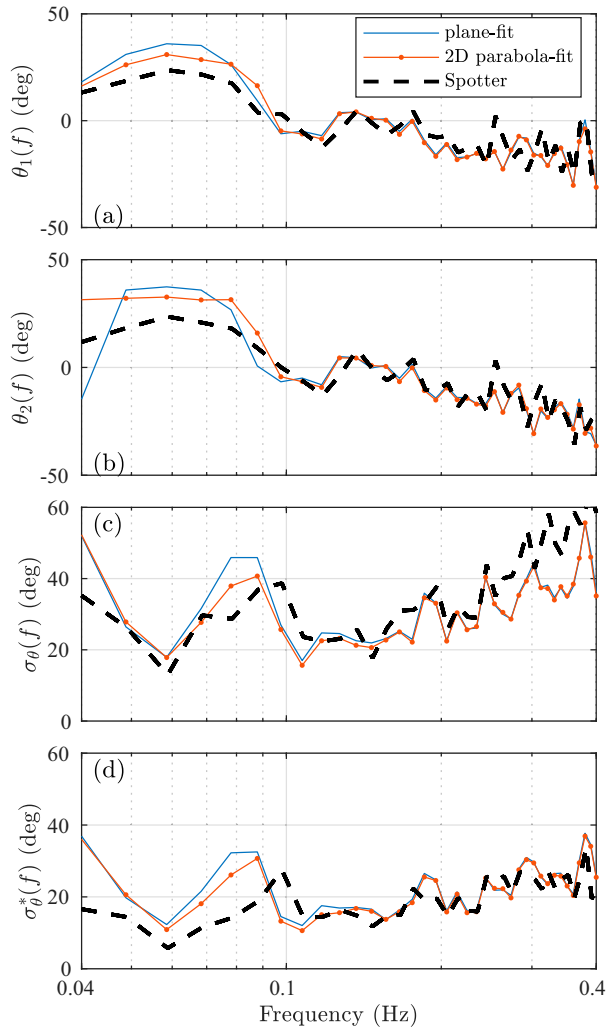


FIG. 10. Mean directions (a) θ_1 [(A7)] and (b) θ_2 [(A8)] and directional spreads (c) $\sigma_\theta(f)$ [(A9)] and (d) $\sigma_\theta^*(f)$ [(A10)] vs frequency for the plane-fit (blue) and 2D parabola-fit (orange) both at $R = 2.4$ m, and Spotter (black).

$\bar{\theta}_{1,\text{swell}} = 28^\circ$, whereas the Spotter has a reduced wave angle $\bar{\theta}_{1,\text{swell}} = 21^\circ$ (Table 1). In the sea band, the 2D parabola-fit $\bar{\theta}_{1,\text{sea}} = -9^\circ$ is quite good with the Spotter $\bar{\theta}_{1,\text{sea}} = -7^\circ$.

For both methods, $\theta_2(f)$ varies from 35° to 0° in the swell band and steadily decreases in the sea band similar to $\theta_1(f)$ (Fig. 10b). In the sea band, $\theta_2(f)$ for both methods is nearly identical and matches well with the Spotter. In the swell band, $\theta_2(f)$ has a larger magnitude than that of the Spotter, with the 2D parabola-fit moderately closer to the Spotter. Even with the relatively large ϵ_{a2} (Fig. 9c), the overall $\theta_2(f)$ compares well with the Spotter in the swell band.

For the plane-fit, the first directional spread estimator $\sigma_\theta(f)$ (A9) is $\approx 20^\circ$ at the $f = 0.06$ Hz $S_\eta(f)$ peak and is larger $\approx 40^\circ$ near $f = 0.085$ Hz where $S_\eta(f)$ is reduced (Fig. 10c). The 2D parabola-fit σ_θ is moderately closer to that of the Spotter. In the sea band, the two estimators and the Spotter $\sigma_\theta(f)$ increase similarly with f , where the Spotter is generally larger than the two

TABLE 1. Energy-weighted bulk wave statistics for the UAS-lidar and Spotter wave buoy: UAS lidar statistics are for $R = 2.4$ m and the 2D parabola-fit method. Shown are wave statistics over the sea–swell (0.04–0.4 Hz) band: Significant height H_s , peak period T_p , energy-weighted mean period \bar{T} , mean direction $\bar{\theta}_1$, and directional spread σ_θ^* . Sea (0.1–0.4 Hz) and swell (0.04–0.1 Hz) mean direction ($\bar{\theta}_{1,\text{sea}}, \bar{\theta}_{1,\text{swell}}$) and directional spread ($\bar{\sigma}_{\theta,\text{sea}}^*, \bar{\sigma}_{\theta,\text{swell}}^*$) are also shown. Energy-weighted statistics are described in the appendix.

	UAS lidar	Spotter wave buoy
H_s (m)	1.24	1.17
T_p (s)	17.0	17.0
\bar{T} (s)	6.2	6.1
$\bar{\theta}_1$ ($^\circ$)	2°	1°
$\bar{\sigma}_\theta^*$ ($^\circ$)	25°	21°
$\bar{\theta}_{1,\text{sea}}$ ($^\circ$)	-9°	-7°
$\bar{\sigma}_{\theta,\text{sea}}^*$ ($^\circ$)	20°	19°
$\bar{\theta}_{1,\text{swell}}$ ($^\circ$)	28°	21°
$\bar{\sigma}_{\theta,\text{swell}}^*$ ($^\circ$)	16°	11°

estimators. The second directional spread estimator $\sigma_\theta^*(f)$ (A10) is $\approx 12^\circ$ at the $f = 0.06$ Hz $S_\eta(f)$ peak and is consistent with the Spotter $\sigma_\theta^* = 10^\circ$ (Fig. 10d). At higher swell-band frequencies where the energy is low, $\sigma_\theta^*(f)$ increases like that of the Spotter. In the sea band, the estimated σ_θ^* generally increases from $\approx 13^\circ$ at $f = 0.1$ Hz to $\approx 25^\circ$ at $f = 0.4$ Hz with some fluctuations. In this band, the Spotter σ_θ^* has a similar pattern increasing from 17° to $\approx 25^\circ$ with few fluctuations. Overall, both $\sigma_\theta(f)$ and $\sigma_\theta^*(f)$ compare well with the Spotter, particularly at frequencies where $S_\eta(f)$ is energetic (Fig. 6), with the 2D parabola-fit performing slightly better. In sum, the results in Figs. 8 and 10 demonstrate the effectiveness of this method in estimating directional properties from a UAS with a mounted multibeam scanning lidar.

6. Energy-weighted (bulk) wave statistics comparison

In sections 4c and 5, we focused on frequency-dependent quantities such as spectra and directional Fourier coefficients. Here, we focus on energy-weighted (or bulk) wave statistics averaged across the sea–swell (0.04–0.4 Hz) band (Table 1). For UAS-lidar statistics, the 2D parabola-fit with $R = 2.4$ m is used. Over the sea–swell band, the UAS-lidar $H_s = 1.24$ m is slightly larger than the Spotter wave buoy $H_s = 1.17$ m, reflecting the slightly lower Spotter wave spectrum (Fig. 6). The UAS-lidar and Spotter peak period are identical at $T_p = 17.0$ s. The energy-weighted UAS-lidar mean period $\bar{T} = 6.2$ s is nearly identical to the Spotter $\bar{T} = 6.1$ s, reflecting the good agreement between the two spectra (Fig. 6). The UAS-lidar sea–swell mean direction $\bar{\theta} = 2^\circ$ is also very close to that of the Spotter $\bar{\theta} = 1^\circ$ (Table 1). The UAS-lidar directional spread in the sea–swell band $\bar{\sigma}_\theta^* = 25^\circ$ is slightly larger than that for the Spotter $\bar{\sigma}_\theta^* = 21^\circ$, consistent with the differences in the $\sigma_\theta^*(f)$ (Fig. 10d). We also examine the directional moments individually in the sea (0.1–0.4 Hz) and swell (0.04–0.1 Hz) bands. The sea-band UAS-lidar $\bar{\theta}_{1,\text{sea}} = -9^\circ$ and $\bar{\sigma}_{\theta,\text{sea}}^* = 20^\circ$ are similar to the Spotter $\bar{\theta}_{1,\text{sea}} = -7^\circ$ and $\bar{\sigma}_{\theta,\text{sea}}^* = 19^\circ$, consistent with the

similar sea-band $\theta_1(f)$ and $\sigma_\theta^*(f)$ for UAS-lidar and Spotter (Figs. 10a,d). The differences in swell-band directional moments between UAS-lidar and Spotter are larger than the sea-band differences, also reflective of the swell-band $\theta_1(f)$ and $\sigma_\theta^*(f)$ UAS-lidar and Spotter differences. The swell-band UAS-lidar $\bar{\theta}_{1,\text{swell}} = 28^\circ$ is larger than the Spotter $\bar{\theta}_{1,\text{swell}} = 21^\circ$ (Table 1), and similarly, the UAS-lidar $\bar{\sigma}_{\theta,\text{swell}}^* = 16^\circ$ is moderately larger than the Spotter $\bar{\sigma}_{\theta,\text{swell}}^* = 11^\circ$. The energy-weighted directional moments have much reduced differences between UAS-lidar and Spotter, as the frequency-averaging reduces the noise in the directional Fourier coefficients. Overall, the good comparison of energy-weighted wave statistics between the UAS-lidar and the Spotter wave buoy demonstrates that the UAS-lidar is an effective tool for estimating wave statistics.

7. Summary and discussion

Here, we have developed and tested a method for estimating directional wave properties analogous to a wave buoy from a UAS with mounted multibeam scanning lidar. The method was tested with an 11-min hover at the location of a Spotter wave buoy on the rocky inner shelf at 10-m water depth offshore of the Monterey Peninsula. For this hover, the UAS can effectively maintain a relatively fixed hover location. The lidar beams were oriented onshore/offshore approximately in the direction of wave propagation. Given the density and distribution of lidar returns even for the largest $R = 2.4$ m (Fig. 2), directional wave properties are likely not sensitive to lidar orientation relative to wave propagation. The method fits either a plane or a 2D parabola to lidar returns within a circular sampling region of radius R varying from 0.8 to 2.4, resulting in estimates of the sea surface and its slope. Requiring at least $N_p = 10$ points within the sampling region leads us to consider radii with $R \geq 0.8$ m. Return and wave statistics are examined as a function of the radius of the sampling region and two methods. Results depend on R and weakly on the method.

Overall, the sea surface elevation spectrum $S_\eta(f)$ comparison between the Spotter and the UAS-lidar is quite good for $R \geq 0.8$ m. This is similar to the accurate wave spectra estimated in the swash zone (Brodie et al. 2015) and across the surfzone (Fiedler et al. 2021). However, our observations are on the inner shelf, seaward of the surfzone, where the lack of foam reduces the number of returns. In addition, the water was untrubid and had a diver-reported visibility of 6 m. Untrubid water also inhibits lidar returns. That $S_\eta(f)$ and directional parameters were so well estimated suggests that the return number was sufficient in this case. It also suggests that this methodology can also be applied to many other ocean regions where waves are not breaking. For tropical waters with 30+ m visibility, the number of lidar returns is likely substantially less and this method may be less useful. A spectral noise floor of $10^{-4} \text{ m}^2 \text{ s}^{-1}$ (Fig. 6) implies that a sea-swell band H_s of ≥ 0.03 m can be measured.

The convergence of the slope spectra $S_{\nabla\eta}(f)$ at larger R and the good comparison with an inferred slope from the Spotter wave buoy indicate that the wave slope is well estimated in the swell band for $R \geq 1.6$ m and in the sea band for all R . Overall, the slope spectra $S_{\nabla\eta}(f)$ are more sensitive to R than $S_\eta(f)$ particularly at the lower and higher frequencies. For $R \geq 1.6$ m, the

swell-band equivalent wave slope $(ak)_{\text{swell}} = 0.0085$ (A2) is very small. This demonstrates the challenge of estimating slope in the swell band and also speaks to the accuracy of the georeferenced lidar data and the ability of the method to accurately fit slopes for larger radii. The swell-band (0.04–0.1 Hz) waves have wavelength varying from 245 to 96 m. For normally incident waves, the array width $2R$ is < 5 m, indicating that swell-band wave slope can still be accurately estimated with such a small array width. At a particular frequency, wavelengths are longer in deep water, so larger radii may be needed in the swell band. This may potentially bias directional estimates due to the lidar beam distribution. The sea-band wave slope $(ak)_{\text{sea}} \approx 0.075$ is an order of magnitude larger than that of the swell band and is similar for all R , suggesting that it is well estimated in this band. The relatively small $(ak)_{\text{sea}}$ also suggests that nonlinearities are weak in this band. In the sea band, the ratio $2R/\lambda$ is always < 0.5 , indicating that the wave slope should not be aliased. In the “chop” band frequencies (0.4–1 Hz), the $R = 0.8$ m 2D parabola-fit matches well the wave buoy inferred slope (Fig. 7b), whereas wave slopes for larger R are reduced substantially due to the low-pass filter effect (or aliasing). Although this comparison is indirect, it suggests that the high-frequency fluctuations in the η and $\partial\eta/\partial x$ time series for $R = 0.8$ m (Fig. 4) are real and not noise. If the wave-buoy-derived slope is accurate in the “chop” (0.4–1 Hz) band, the georeferenced lidar data and this methodology may also be useful in inferring wave properties in the chop band. In regions where wave fronts are very steep, such as surfzone bores, this method for estimating slope spectra may have errors.

Directional Fourier coefficients are computed from $S_\eta(f)$, the individual components of slope spectra, and their cross-spectra, all of which have signal and noise. All four coefficients compared well to the Spotter in the sea band, and only $a_2(f)$ did not perform well in the swell band. This is likely due to the functional form of $a_2(f)$ which depends on the difference in the x and y slope spectra $S_{\eta_x}(f) - S_{\eta_y}(f)$ (A5), which if the signal-to-noise ratio is low would bias $a_2(f)$ low. Only $a_2(f)$ has a difference in the numerator (A3)–(A6), and thus, only $a_2(f)$ is expected to have this bias due to low signal-to-noise ratio. In the swell band, slopes are very small, and thus, the spectral signal-to-noise ratio is reduced, which when subtracted (A5) could bias $a_2(f)$ low in the swell band. Generally, the signal-to-noise ratio of the spectra depends on the particular wave conditions. From 0.04 to 0.25 Hz, the 2D parabola-fit at the largest $R = 2.4$ m gave the best results. In the sea band, the comparison of directional moments (Fig. 10) was quite good. In the swell band, the magnitude of the mean wave angle and the directional spreads were larger than that of the Spotter.

In the discussion between UAS-lidar derived and Spotter quantities, we have not explicitly considered the errors of the Spotter wave buoy. The Spotter wave buoy has only been compared to Datawell wave buoys across from 0.05 to 0.3 Hz (Raghukumar et al. 2019), although we show Spotter wave buoy results out to 1 Hz. Thus, any conclusions based on comparison with Spotter between 0.3 and 1 Hz are tentative. The differences in wave spectra between Spotter and Datawell Waverider buoys (Raghukumar et al. 2019) are consistent with the differences observed here (Fig. 6). Mean wave direction (energy weighted 0.05–0.3 Hz) has rms differences to a Waverider buoy of $\approx 5^\circ$,

consistent with the differences observed here in the sea band. More recently, wave buoys were compared to a fixed-location pressure sensor array over a 3-month period (Collins et al. 2024). This comparison was performed across a low-frequency band (0.035–0.065 Hz), a mid-frequency band (0.065–0.165 Hz), and a high-frequency band (0.165–0.26 Hz). Overall, the Spotter wave height and wave direction are compared well to those of the pressure sensor array in the mid- to high-frequency bands. This is consistent with our good comparison in the sea band. However, in the low-frequency band, the Spotter wave buoy had significant differences in wave height and wave angles relative to the pressure sensor array. In particular, root-mean-square wave angle errors were 8° (Collins et al. 2024), which is consistent with the swell-band $\bar{\theta}_{1,\text{swell}}$ differences of 7° between the UAS-lidar and Spotter (Table 1 and Figs. 10a,b). It is thus unclear whether the UAS-lidar or Spotter wave angle is more accurate in the swell band. Overall, the internal consistency of the UAS-lidar-derived results and their good comparison to the Spotter wave buoy demonstrate that this is an effective tool for estimating wave statistics.

Acknowledgments. This paper is part of the ROcky Shore: eXperiment and SIMulations (ROXSI) project, funded by the Office of Naval Research through Grants N000142112786 and N0001423WX01357. The Monterey NOAA Sanctuary, CA Fish and Wildlife, and Pebble Beach provided environmental permission for the experiment with permitting support provided by Chris Miller. We thank the SIO and NPS field crews for their invaluable support with the field experiment; for SIO: Brian Woodward, Kent Smith, Rob Grenzeback, Lucian Parry, Shane Finnerty, Carson Black, Duncan Wheeler, Annie Adelson, Loren Clark, Kaden Quinn, and Kanoa Pick; for NPS: Paul Jessen, Charlotte Benbow, Pat Collins, Mike Cook, Matt Gough, and Ian Jenstrom. We appreciate the valuable discussions with the ROXSI team that informed this manuscript. Julia Fiedler and Alex Simpson provided valuable comments and feedback on the manuscript.

Data availability statement. The data and processing, analysis, and figure generation scripts presented in this paper available at the Zenodo.org data repository (<https://doi.org/10.5281/zenodo.10420808>).

APPENDIX

Dispersion Relationship, Directional Fourier Coefficients, and Directional Moments

For reference, the linear dispersion relationship for surface gravity waves is

$$\omega = \sqrt{gk \tanh(kh)}, \quad (\text{A1})$$

where $\omega = 2\pi f$ is the wave radian frequency, g is the gravity, k is the wavenumber, and h is the still water depth. In wave theory, the monochromatic wave slope ak is a standard measure of wave nonlinearity. From the slope spectra, an equivalent swell- and sea-band ak is calculated as

$$(ak)_{\text{swell}} = \sqrt{2 \int_{\text{swell}} S_{|\nabla \eta|} df}, \quad (\text{A2})$$

where the swell band is $0.04 \leq f < 0.1$ Hz. Similarly, $(ak)_{\text{sea}}$ is defined over the $0.1 \leq f < 0.4$ Hz band and $(ak)_{\text{chop}}$ is defined over the $0.4 \leq f < 1$ Hz band.

We define the directional moments used to calculate the mean wave angle $\theta(f)$ and directional spread $\sigma_\theta(f)$. As in the text, sea surface elevation spectra are given by $S_\eta(f)$ and cross-shore and alongshore slope spectra are given by $S_{\eta_x}(f)$ and $S_{\eta_y}(f)$, respectively. The cospectrum (real part of the cross-spectrum) between η_x and η_y is given by $C_{\eta_x \eta_y}(f)$. The quad-spectrum (imaginary part of the cross-spectrum) between η and η_x is defined as $Q_{\eta \eta_x}(f)$ and similarly between η and η_y . With these definitions, the directional moments are (e.g., Longuet-Higgins et al. 1963; Kuik et al. 1988; Herbers et al. 1999)

$$a_1(f) = \frac{\int_{-\pi}^{\pi} \cos(\theta) E(f, \theta) d\theta}{\int_{-\pi}^{\pi} E(f, \theta) d\theta} = \frac{-Q_{\eta \eta_x}(f)}{\{S_\eta(f)[S_{\eta_x}(f) + S_{\eta_y}(f)]\}^{1/2}}, \quad (\text{A3})$$

$$b_1(f) = \frac{\int_{-\pi}^{\pi} \sin(\theta) E(f, \theta) d\theta}{\int_{-\pi}^{\pi} E(f, \theta) d\theta} = \frac{-Q_{\eta \eta_y}(f)}{\{S_\eta(f)[S_{\eta_x}(f) + S_{\eta_y}(f)]\}^{1/2}}, \quad (\text{A4})$$

$$a_2(f) = \frac{\int_{-\pi}^{\pi} \cos(2\theta) E(f, \theta) d\theta}{\int_{-\pi}^{\pi} E(f, \theta) d\theta} = \frac{S_{\eta_x}(f) - S_{\eta_y}(f)}{S_{\eta_x}(f) + S_{\eta_y}(f)}, \quad (\text{A5})$$

$$b_2(f) = \frac{\int_{-\pi}^{\pi} \sin(2\theta) E(f, \theta) d\theta}{\int_{-\pi}^{\pi} E(f, \theta) d\theta} = \frac{2C_{\eta_x \eta_y}(f)}{S_{\eta_x}(f) + S_{\eta_y}(f)}. \quad (\text{A6})$$

The directional moments, such as mean wave angle and directional spread, are functions of the Fourier coefficients (e.g., Kuik et al. 1988):

$$\theta_1(f) = \tan^{-1} \left[\frac{b_1(f)}{a_1(f)} \right], \quad (\text{A7})$$

$$\theta_2(f) = 0.5 \tan^{-1} \left[\frac{b_2(f)}{a_2(f)} \right], \quad (\text{A8})$$

$$\sigma_\theta(f) = \sqrt{2\{1 - a_1(f)\cos[\theta_1(f)] - b_1(f)\sin[\theta_1(f)]\}}, \quad (\text{A9})$$

$$\sigma_\theta^*(f) = \sqrt{0.5\{1 - a_2(f)\cos[2\bar{\theta}_1(f)] - b_2(f)\sin[2\bar{\theta}_1(f)]\}}. \quad (\text{A10})$$

These directional moments are in radians and converted to degrees. We also estimate the mean wave angle averaged over the sea and swell band from energy-weighted directional Fourier coefficients, i.e., for the swell-band $\bar{a}_{1,\text{swell}}$,

$$\bar{a}_{1,\text{swell}} = \frac{\int_{\text{swell}} a_1(f)S(f)df}{\int_{\text{swell}} S(f)df}, \quad (\text{A11})$$

and similarly for the other Fourier coefficients. The mean wave angle in the swell (or sea) band is then defined as

$$\bar{\theta}_{1,\text{swell}} = \tan^{-1}\left(\frac{\bar{b}_{1,\text{swell}}}{\bar{a}_{1,\text{swell}}}\right). \quad (\text{A12})$$

REFERENCES

- Almeida, L. P., G. Masselink, P. Russell, M. Davidson, T. Poate, R. McCall, C. Blenkinsopp, and I. Turner, 2013: Observations of the swash zone on a gravel beach during a storm using a laser-scanner (lidar). *J. Coastal Res.*, **65**, 636–641, <https://doi.org/10.2112/SI65-108.1>.
- Baker, C. M., M. Moulton, M. L. Palmsten, K. Brodie, E. Nuss, and C. C. Chickadel, 2023: Remotely sensed short-crested breaking waves in a laboratory directional wave basin. *Coastal Eng.*, **183**, 104327, <https://doi.org/10.1016/j.coastaleng.2023.104327>.
- Blenkinsopp, C. E., M. A. Mole, I. L. Turner, and W. L. Peirson, 2010: Measurements of the time-varying free-surface profile across the swash zone obtained using an industrial LIDAR. *Coastal Eng.*, **57**, 1059–1065, <https://doi.org/10.1016/j.coastaleng.2010.07.001>.
- , I. L. Turner, M. J. Allis, W. L. Peirson, and L. E. Garden, 2012: Application of LiDAR technology for measurement of time-varying free-surface profiles in a laboratory wave flume. *Coastal Eng.*, **68**, 1–5, <https://doi.org/10.1016/j.coastaleng.2012.04.006>.
- Branch, R. A., and Coauthors, 2018: Airborne LiDAR measurements and model simulations of tides, waves, and surface slope at the mouth of the Columbia River. *IEEE Trans. Geosci. Remote Sens.*, **56**, 7038–7048, <https://doi.org/10.1109/TGRS.2018.2847561>.
- Brodie, K. L., B. Raubenheimer, S. Elgar, R. K. Slocum, and J. E. McNinch, 2015: Lidar and pressure measurements of inner-surfzone waves and setup. *J. Atmos. Oceanic Technol.*, **32**, 1945–1959, <https://doi.org/10.1175/JTECH-D-14-00222.1>.
- , B. L. Bruder, R. K. Slocum, and N. J. Spore, 2019: Simultaneous mapping of coastal topography and bathymetry from a lightweight multicamera UAS. *IEEE Trans. Geosci. Remote Sens.*, **57**, 6844–6864, <https://doi.org/10.1109/TGRS.2019.2909026>.
- Collins, C. O., and Coauthors, 2024: Performance of moored GPS wave buoys. *Coastal Eng. J.*, **66**, 17–43, <https://doi.org/10.1080/21664250.2023.2295105>.
- Feddersen, F., A. M. Fincham, K. L. Brodie, A. D. Young, M. S. Spydell, D. J. Grimes, M. Pieszka, and K. Hanson, 2023: Cross-shore wind-induced changes to field-scale overturning wave shape. *J. Fluid Mech.*, **958**, A4, <https://doi.org/10.1017/jfm.2023.40>.
- , A. Amador, K. Pick, A. Vizuet, K. Quinn, E. Wolfinger, J. H. MacMahan, and A. Fincham, 2024: The wavedrifter: A low-cost IMU-based Lagrangian drifter to observe steepening and overturning of surface gravity waves and the transition to turbulence. *Coastal Eng. J.*, **66**, 44–57, <https://doi.org/10.1080/21664250.2023.2238949>.
- Fiedler, J. W., K. L. Brodie, J. E. McNinch, and R. T. Guza, 2015: Observations of runup and energy flux on a low-slope beach with high-energy, long-period ocean swell. *Geophys. Res. Lett.*, **42**, 9933–9941, <https://doi.org/10.1002/2015GL066124>.
- , L. Kim, R. L. Grenzeback, A. P. Young, and M. A. Merrifield, 2021: Enhanced surf zone and wave runup observations with hovering drone-mounted lidar. *J. Atmos. Oceanic Technol.*, **38**, 1967–1978, <https://doi.org/10.1175/JTECH-D-21-0027.1>.
- Herbers, T. H. C., and S. J. Lentz, 2010: Observing directional properties of ocean swell with an Acoustic Doppler Current Profiler (ADCP). *J. Atmos. Oceanic Technol.*, **27**, 210–225, <https://doi.org/10.1175/2009JTECHO681.1>.
- , S. Elgar, and R. T. Guza, 1999: Directional spreading of waves in the nearshore. *J. Geophys. Res.*, **104**, 7683–7693, <https://doi.org/10.1029/1998JC900092>.
- , P. F. Jessen, T. T. Janssen, D. B. Colbert, and J. H. MacMahan, 2012: Observing ocean surface waves with GPS-tracked buoys. *J. Atmos. Oceanic Technol.*, **29**, 944–959, <https://doi.org/10.1175/JTECH-D-11-00128.1>.
- Huang, Z.-C., C.-Y. Yeh, K.-H. Tseng, and W.-Y. Hsu, 2018: A UAV-RTK lidar system for wave and tide measurements in coastal zones. *J. Atmos. Oceanic Technol.*, **35**, 1557–1570, <https://doi.org/10.1175/JTECH-D-17-0199.1>.
- Hwang, P. A., D. W. Wang, E. J. Walsh, W. B. Krabill, and R. N. Swift, 2000: Airborne measurements of the wavenumber spectra of ocean surface waves. Part I: Spectral slope and dimensionless spectral coefficient. *J. Phys. Oceanogr.*, **30**, 2753–2767, [https://doi.org/10.1175/1520-0485\(2001\)031<2753:AMOTWS>2.0.CO;2](https://doi.org/10.1175/1520-0485(2001)031<2753:AMOTWS>2.0.CO;2).
- Irish, J. L., J. M. Wozencraft, A. G. Cunningham, and C. Giroud, 2006: Nonintrusive measurement of ocean waves: Lidar wave gauge. *J. Atmos. Oceanic Technol.*, **23**, 1559–1572, <https://doi.org/10.1175/JTECH1936.1>.
- Kuik, A. J., G. P. Van Vledder, and L. H. Holthuijsen, 1988: A method for the routine analysis of pitch-and-roll buoy wave data. *J. Phys. Oceanogr.*, **18**, 1020–1034, [https://doi.org/10.1175/1520-0485\(1988\)018%3C1020:AMFTRA%3E2.0.CO;2](https://doi.org/10.1175/1520-0485(1988)018%3C1020:AMFTRA%3E2.0.CO;2).
- Lange, A. M. Z., J. W. Fiedler, M. A. Merrifield, and R. T. Guza, 2023: UAV video-based estimates of nearshore bathymetry. *Coastal Eng.*, **185**, 104375, <https://doi.org/10.1016/j.coastaleng.2023.104375>.
- Lenain, L., and W. K. Melville, 2017: Measurements of the directional spectrum across the equilibrium saturation ranges of wind-generated surface waves. *J. Phys. Oceanogr.*, **47**, 2123–2138, <https://doi.org/10.1175/JPO-D-17-0017.1>.
- , and N. Pizzo, 2021: Modulation of surface gravity waves by internal waves. *J. Phys. Oceanogr.*, **51**, 2735–2748, <https://doi.org/10.1175/JPO-D-20-0302.1>.
- , N. M. Statom, and W. K. Melville, 2019: Airborne measurements of surface wind and slope statistics over the ocean. *J. Phys. Oceanogr.*, **49**, 2799–2814, <https://doi.org/10.1175/JPO-D-19-0098.1>.
- Longuet-Higgins, M. S., D. Cartwright, and N. Smith, 1963: Observations of the directional spectrum of sea waves using the motions of a floating buoy. *Ocean Wave Spectra*, Prentice Hall, 111–136.
- Martins, K., C. E. Blenkinsopp, H. E. Power, B. Bruder, J. A. Puleo, and E. W. J. Bergsma, 2017: High-resolution monitoring of wave transformation in the surf zone using a LiDAR

- scanner array. *Coastal Eng.*, **128**, 37–43, <https://doi.org/10.1016/j.coastaleng.2017.07.007>.
- Melville, W. K., L. Lenain, D. R. Cayan, M. Kahru, J. P. Kleissl, P. F. Linden, and N. M. Statom, 2016: The modular aerial sensing system. *J. Atmos. Oceanic Technol.*, **33**, 1169–1184, <https://doi.org/10.1175/JTECH-D-15-0067.1>.
- O’Dea, A., K. Brodie, and S. Elgar, 2021: Field observations of the evolution of plunging-wave shapes. *Geophys. Res. Lett.*, **48**, e2021GL093664, <https://doi.org/10.1029/2021GL093664>.
- Oltman-Shay, J., and R. T. Guza, 1984: A data-adaptive ocean wave directional-spectrum estimator for pitch and roll type measurements. *J. Phys. Oceanogr.*, **14**, 1800–1810, [https://doi.org/10.1175/1520-0485\(1984\)014<1800:ADAOWD>2.0.CO;2](https://doi.org/10.1175/1520-0485(1984)014<1800:ADAOWD>2.0.CO;2).
- Rabault, J., and Coauthors, 2022: OpenMetBuoy-v2021: An easy-to-build, affordable, customizable, open-source instrument for oceanographic measurements of drift and waves in sea ice and the open ocean. *Geosciences*, **12**, 110, <https://doi.org/10.3390/geosciences12030110>.
- Raghukumar, K., G. Chang, F. Spada, C. Jones, T. Janssen, and A. Gans, 2019: Performance characteristics of “spotter,” a newly developed real-time wave measurement buoy. *J. Atmos. Oceanic Technol.*, **36**, 1127–1141, <https://doi.org/10.1175/JTECH-D-18-0151.1>.
- Turner, I. L., M. D. Harley, and C. D. Drummond, 2016: UAVS for coastal surveying. *Coastal Eng.*, **114**, 19–24, <https://doi.org/10.1016/j.coastaleng.2016.03.011>.
- Wojtanowski, J., M. Zygmunt, M. Kaszczuk, Z. Mierczyk, and M. Muzal, 2014: Comparison of 905 nm and 1550 nm semiconductor laser rangefinders’ performance deterioration due to adverse environmental conditions. *Opto-Electron. Rev.*, **22**, 183–190, <https://doi.org/10.2478/s11772-014-0190-2>.